

PAPER • OPEN ACCESS

Layered high-entropy sulfides: boosting electrocatalytic performance for hydrogen evolution reaction by cocktail effects










To cite this article: Ling Lin *et al* 2024 *Mater. Futures* **3** 045102

View the [article online](#) for updates and enhancements.

You may also like

- [The development of a high throughput drug-responsive model of white adipose tissue comprising adipogenic 3T3-L1 cells in a 3D matrix](#)
Alexander D Graham, Rajesh Pandey, Viktoriya S Tsancheva et al.
- [Recent progress and future prospects of high-entropy materials for battery applications](#)
Wenbo Qiu, Zidong Wang, Shijiang He et al.
- [Self-Discharge of Heterogeneous Electrochemical Supercapacitor of PbO₂/H₂SO₄/C Related to Manganese and Titanium Ions](#)
S. A. Kazaryan, S. V. Litvinenko and G. G. Kharisov

Layered high-entropy sulfides: boosting electrocatalytic performance for hydrogen evolution reaction by cocktail effects

Ling Lin¹ , Ziming Ding¹ , Guruprakash Karkera² , Thomas Diemant² , Dong-Hui Chen³ , Maximilian Fichtner^{1,2} , Horst Hahn^{1,4} , Jasmin Aghassi-Hagmann¹, Ben Breitung^{1,*}  and Simon Schweidler^{1,*} 

¹ Institute of Nanotechnology, Karlsruhe Institute of Technology, Kaiserstraße 12, 76131 Karlsruhe, Germany

² Helmholtz Institute Ulm, Helmholtzstraße 11, 89081 Ulm, Germany

³ Institute of Functional Interfaces, Karlsruhe Institute of Technology, Kaiserstraße 12, 76131 Karlsruhe, Germany

⁴ School of Sustainable Chemical, Biological and Materials Engineering, University of Oklahoma, 100 E. Boyd St, Norman, OK 73019, United States of America

E-mail: ben.breitung@kit.edu and simon.schweidler@kit.edu

Received 19 July 2024, revised 2 October 2024

Accepted for publication 21 October 2024

Published 7 November 2024



CrossMark

Abstract

This study explores high-entropy sulfides (HESs) as potential electrocatalysts for the hydrogen evolution reaction (HER). Novel *Pa-3* and *Pnma* structured HESs containing Fe, Mn, Ni, Co and Mo, were synthesized via a facile mechanochemical method. Structural and chemical properties were extensively characterized using x-ray diffraction, transmission electron microscopy, energy-dispersive x-ray spectroscopy, and x-ray photoelectron spectroscopy. The electrocatalytic performance of four as-prepared HESs in alkaline electrolyte for HER reveals the remarkable outperformance compared to medium-entropy and conventional sulfides. Particularly, $(\text{Fe}_{0.2}\text{Mn}_{0.2}\text{Ni}_{0.2}\text{Co}_{0.2}\text{Mo}_{0.2})\text{S}_2$ demonstrated outstanding activities, with minimal overpotentials (187 mV at 10 mA cm⁻²) and outstanding durability under harsh alkaline conditions (a mere polarization increase $\Delta E = 17$ mV after 14 h via chronopotentiometry). The remarkable catalytic activities can be attributed to synergistic effects resulting from the cocktail effects within the high-entropy disulfide. The introduction of Mo contributes to the formation of a layered structure, which leads to an increased surface area and thus to a superior HER performance compared to other HES and conventional sulfides. This work demonstrates the promising potential of HES and underscores that further development for catalytic applications paves the way for innovative routes to new and more efficient active materials for HER catalysis.

* Authors to whom any correspondence should be addressed.



Original content from this work may be used under the terms of the [Creative Commons Attribution 4.0 licence](https://creativecommons.org/licenses/by/4.0/). Any further distribution of this work must maintain attribution to the author(s) and the title of the work, journal citation and DOI.

Supplementary material for this article is available [online](#)

Keywords: high-entropy materials, high-entropy sulfides, hydrogen evolution reaction

1. Introduction

Hydrogen, with its clean and renewable nature, offers an ideal alternative to fossil fuels in various industries and applications, such as transportation, steelmaking, and power generation. It serves as a pivotal element in the transition towards a sustainable energy future. In this context, electrochemical water splitting is a clean and promising method for the production of hydrogen gas, which has attracted widespread attention [1]. Electrochemical water splitting involves two reactions: the hydrogen evolution reaction (HER) at the cathode and the oxygen evolution reaction (OER) at the anode [2]. The development of efficient and cost-effective catalysts to reduce energy consumption in water electrolysis is crucial for the commercialization of this process.

The Pt-group elements have proven to be the most effective HER electrocatalysts in the past, but their high cost and limited earth abundance hinder their widespread commercial use [3]. Therefore, much attention has shifted to abundant, non-precious metal electrocatalysts, such as Ni, Co, Fe and Mo, as alternative materials [4]. One notable example, where the morphology and structure especially supports catalytic activity, is MoS₂, which, due to its layered crystal and distinct electronic structure, has prompted extensive research for its application in HER [5–8].

Recently, notable research has been devoted to high-entropy sulfides (HESs) based on multiple transition metals, exploring their potential as catalysts for water electrolysis. However, most of these studies have primarily focused on catalyzing OER [9–13]. In 2022, Lei *et al* reported the good catalytic activity and stability of carbon-supported CoZnCdCuMnS@CF (CF = carbon fiber) for overall water splitting in alkaline medium [14], which was also the first study related to the application of HESs in HER electrocatalysis. In the study by Xiao *et al* excellent electrocatalytic performance for the HER using HESs was also demonstrated, highlighting the impact of the high-entropy concept itself [15]. The seven-metal-containing HES (AgCuZnMnCoInGa)S exhibited the best HER activity, which was attributed to the high-entropy nature of the material.

The high-entropy concept allows the incorporation of multiple elements in a single-phase structure with an almost infinite number of possible compositional combinations. This approach leads to a unique surface of the catalyst and exceptional flexibility, allowing for tailoring of material properties, resulting in enhanced stability, improved conductivity, and optimized catalytic performance. In addition, the cocktail effects, which describe the interaction of multiple elements within the high-entropy materials (HEMs), offer synergistic advantages, leading to highly tailorable electrochemical properties and increasing interest in electrocatalytic applications.

Furthermore, transition metal sulfides in general have shown great potential in environmental applications, such as pollutant degradation [16, 17] and water purification [18], due to their structural diversity and ability to accommodate various active sites. This versatility makes HES not only valuable for electrocatalysis but also for broader environmental applications, enhancing their sustainability impact.

In this study, various HESs with either *Pa-3* or *Pnma* structure were synthesized using high-energy ball-milling and comprehensively characterized by x-ray diffraction (XRD), inductively coupled plasma optical emission spectroscopy (ICP-OES), transmission electron microscopy (TEM), energy dispersive x-ray (EDX) spectroscopy, x-ray photoelectron spectroscopy (XPS), and attenuated total reflection-infrared (ATR-IR) spectroscopy. Additionally, the impact of Mo, as an inexpensive and non-critical element in such high-entropy structures, was investigated in detail. Medium-entropy sulfides (MESs), conventional sulfides and state-of-the-art catalysts (e.g. Pt/C) were used as reference materials for comparison using a standard three-electrode electrochemical setup in an alkaline electrolyte. The results show that the cocktail effects have significantly influenced both the structure and catalytic performance of HESs, demonstrating the overall advantage of the high-entropy approach. Furthermore, this research work highlights not only the potential and capabilities of HESs in electrocatalysis, but also the promising application of the high-entropy approach for targeted tailoring of material properties for electrochemical water splitting. Overall, these findings underscore the critical role of molybdenum, the metal-to-sulfur ratio, and the high-entropy concept in enhancing the structural and catalytic properties of HES materials. The ability to tune the metal-to-sulfur ratio offers a pathway to optimize both the structural configuration and catalytic performance, particularly in HER applications. This study highlights the importance of controlling composition to harness the full potential of high-entropy systems in electrocatalysis. To the best of our knowledge, this is the first time this structural adaptation has been observed in HESs, further highlighting the unique potential of HEMs in electrocatalysis.

2. Methods

2.1. Synthesis

All reagents were purchased from commercial sources (Sigma Aldrich/Alfa Aesar, purity $\geq 99\%$) and used without further purification. MS, MS2 and 4MS2 were prepared by a high-energy planetary ball-milling process, more details can be found elsewhere [19]. MS2-Mo was obtained by ball milling over 110 h using FeS₂, MnS, Ni₃S₂, CoS₂, MoS₂ and

sulfur powder in the respective metal to sulfur ratios. MS-Mo was prepared by ball milling for 60 h by mixing FeS, MnS, Ni₃S₂, CoS₂, MoS₂ and sulfur powder in the respective metal-to-sulfur ratios. All products were synthesized in a high-energy planetary ball-milling machine (Retsch PM 100, Retsch GmbH) at 500 rpm using 50 ml WC vials and 5 mm diameter WC balls under argon atmosphere. The weight ratio of balls to materials was 40:1.

2.2. Materials characterization

XRD patterns were collected from powder samples at room temperature, using a STOE Stadi P diffractometer with Ga-jet x-ray source (Ga-K_β radiation, 1.2079 Å). Refinement of the XRD patterns was performed using TOPAS Academics V5 software. Si served as a calibration sample to determine the instrumental resolution. Background refinement was done using a linear interpolation function comprising 36 parameters.

The samples for ICP-OES were dissolved in aqua regia (HCl: HNO₃, 3:1) and analysed by performing a double determination using an ARCOS ICP-OES (Spectro Analytical Instruments, Kleve, Germany) with axial plasma view.

TEM measurements, including selected area electron diffraction (SAED), high-resolution TEM (HR-TEM) and scanning TEM—energy-dispersive x-ray spectroscopy (STEM-EDX), were performed on a ThermoScientific Themis 300 microscope, equipped with a high angle angular dark field-STEM detector and Super-X EDX detector. The microscope was operated at an accelerating voltage of 300 kV. The powdered samples were spread onto a gold grid coated with holey carbon and then placed onto an FEI double tilt holder.

XPS measurements were conducted using a Phoibos 150 spectrometer system (Specs) with monochromatized Al K_α radiation (400 W, 15 kV). The pass energies at the analyzer were set to 90 and 30 eV for survey and detail measurements, respectively. To calibrate the binding energy, the C 1 s peak of adventitious carbon was used and set to 284.8 eV. Peak fitting was performed with CasaXPS software, using Gaussian-Lorentzian peak shapes and the expected values for intensity ratios and spin-orbit-splittings of the S 2p and Mo 3 d peak doublets [20]. To account for the contribution of S 2 s peaks from different S species in the Mo 3d detail spectra, corresponding peaks were entered. The positions of these S 2 s peaks were fixed by assuming a constant distance of 64.4 eV between the S 2p_{3/2} and S 2 s peak (known from previous work with MoS₂). The intensities were related to the S 2p peaks, taking into consideration the relative sensitivity factors of the S 2p and S 2 s peaks. ATR-IR spectroscopy measurements were performed on an ALPHA FT-IR spectrometer (Bruker) in the range from 600–4000 cm⁻¹. All spectra were background corrected using the OPUS software.

2.3. Electrochemistry

Electrochemical measurements were conducted using a three-electrode setup on a modulated speed rotator (Equilibrium SAS) with a rotating glassy carbon working electrode

(area = 0.196 cm²) at a rotation speed of 1600 rpm. A graphite rod and Hg/HgO were used as counter and reference electrodes, respectively. For the preparation of the working electrodes, a solution of 8 mg of the active material and 2 mg carbon black (Super P Conductive, 99+ %, Alfa Aesar) in a mixture of 1800 μl of 2-propanol, 100 μl of H₂O and 100 μl of Nafion was prepared. An uniform ink was obtained by sonicating in an ice water bath for 30 min in an ultrasonic finger/homogenizer. Subsequently, 16.5 μl of the solution was dropped onto the surface of the glassy carbon working electrode and dried, resulting in a catalyst loading of 0.33 mg cm⁻². Platinum on graphitized carbon (Pt/C, 20 wt. % Pt loading, Sigma Aldrich) was used as commercial HER catalyst reference. All measurements were performed in an N₂-saturated 1 M KOH electrolyte at room temperature by a potentiostat (BioLogic GmbH). Linear sweep voltammetry (LSV) was conducted at a sweep rate of 5 mV s⁻¹ in a potential range from 0.1 to -0.6 V vs. reversible hydrogen electrode (RHE). The measured potentials are referred to the RHE, $E_{\text{RHE}} = E_{\text{Hg/HgO}} + 0.059 \times \text{pH} + 0.098 \text{ V}$. The pH of the electrolyte was determined by a pH meter to be 13.3. All LSV results were 85% IR-corrected. The overpotential $\eta = 0 - E_{\text{RHE}}$. Electrochemical impedance spectroscopy (EIS) measurements were carried out at an overpotential of 317 mV in a frequency range from 1 to 100 kHz with an alternating current amplitude of 10 mV. The double-layer capacitance (C_{dl}) was evaluated via cyclic voltammetry (CV) measured at five different scan rates (5, 10, 20, 40 and 60 mV s⁻¹) in the non-Faradaic potential range from 0.282 V to 0.182 V vs. RHE. The electrical chemical surface area (ECSA) was calculated assuming that the capacitance of a flat surface (C_s) is ~40 μF for 1 cm² on a real surface area, then the ECSA is estimated as $\text{ECSA} = C_{\text{dl}}/C_{\text{s}}$. The stability of samples was compared by chronopotentiometry at the constant current density of -10 mA cm⁻². The long-term stability of MS2-Mo was also assessed by performing 100, 1000, 2000, 5000, and 8000 CV continuous scans between 0.10 and -0.42 V vs. RHE at the scan rate of 100 mV s⁻¹.

3. Results and discussion

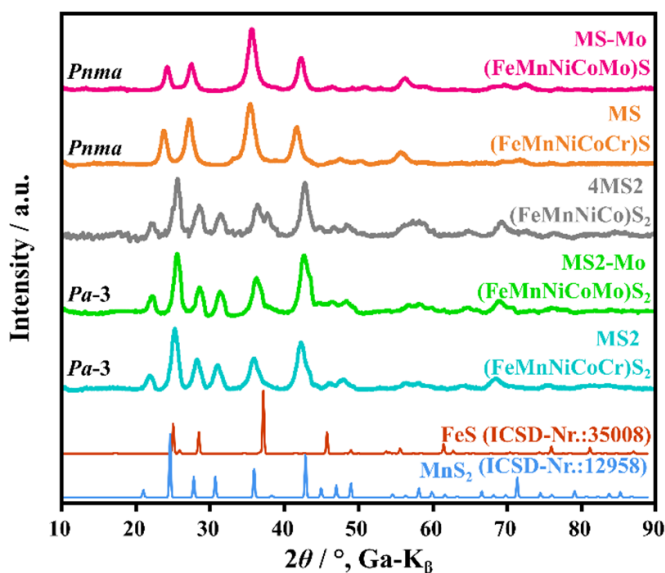
Novel catalyst materials were synthesized using a straightforward high-energy ball-milling method in an inert atmosphere, resulting in the successful preparation of HESs with distinct crystallographic structures. The HESs consist of five transition metals Fe, Mn, Ni, and Co as a base, combined with either Cr or Mo, each in equimolar ratios.

The stoichiometric composition of the synthesized materials was determined using ICP-OES, and the results, along with the abbreviations used later in the study, are provided in table 1.

For crystal structure evaluation, XRD measurements were performed. Figure 1 shows the comparison of the XRD patterns for all prepared materials. In addition to MS, MS-Mo, MS2 and MS2-Mo, a MES containing only four transition metals, referred to as 4MS2 (FeMnNiCo)S₂, is also included [19]. The phase of the high-entropy monosulfides (MS-Mo and MS) and the high-entropy disulfides (MS2-Mo and MS2)

Table 1. ICP-OES results and abbreviations of the synthesized HESs materials.

Structure formula	Material
(Fe _{0.21} Mn _{0.21} Ni _{0.21} Co _{0.20} Cr _{0.21})S ₁	MS
(Fe _{0.17} Mn _{0.16} Ni _{0.17} Co _{0.18} Mo _{0.17})S ₁	MS-Mo
(Fe _{0.22} Mn _{0.20} Ni _{0.20} Co _{0.20} Cr _{0.20})S ₂	MS2
(Fe _{0.20} Mn _{0.20} Ni _{0.20} Co _{0.20} Mo _{0.20})S ₂	MS2-Mo

**Figure 1.** Comparison of XRD patterns of all as-synthesized sulfides used as HER catalysts. The data are background corrected.

show a pure orthorhombic (space group = *Pnma*) or cubic (space group = *Pa-3*) crystal structure, respectively, which is related to the ratio of metal and sulfur near to 1:1 or 1:2. The 4MS2 also primarily exhibits a cubic *Pa-3* structure, although a few impurity peaks from secondary phases are detected (figure 1).

The Rietveld refinement of MS-Mo and MS2-Mo is shown in figure S1. The result of MS-Mo confirms the *Pnma* phase, with a unit cell volume of 108.8(3) Å³ and lattice parameters of $a = 5.462(2)$ Å, $b = 3.388(5)$ Å, and $c = 5.876(1)$ Å. The refinement of MS2-Mo indicates a pure *Pa-3* phase with $V = 181.8(4)$ Å³ and $a = 5.666(4)$ Å. A comparison between the structures can be found in table S1 [19].

The Mo source for the synthesis process was commercial MoS₂, showing a *P6₃/mmc* structure in the XRD pattern (figure S2). MoS₂ is known to appear in three different structures, one belonging to a hexagonal crystal system (2H-MoS₂) and the other to a trigonal crystal system (3R-MoS₂) [21]. The third reported structure is a crystal system (1T-MoS₂), but it appears to be metastable and it is difficult to be prepared on a large scale by conventional methods. Nevertheless, due to a high electrical conductivity, 1T-MoS₂ is an attractive electrocatalyst for HER [22–26]. Despite these structural discrepancies towards the *Pnma* and *Pa-3* structure of the prepared HESs, Mo could be incorporated into the

respective orthorhombic and cubic crystal systems without forming additional phases (figures 1 and S1). This is noteworthy, as such structures have not been previously reported for molybdenum sulfides.

The HER performance of the various HESs was tested using a standard three-electrode setup in N₂-saturated 1 M KOH electrolyte solution. To enhance the electronic conductivity, all materials were mixed with carbon black in a weight ratio of 4:1 and directly used as active materials (for more details please refer to the **experimental section**). Polarization curves of all HESs and commercial 20 wt.% Pt/C were performed by LSV and are shown in figure 2(a). To compare the HER reaction kinetics, Tafel slopes were derived from the corresponding LSV curves which are plotted in figure 2(b). The reference catalyst Pt/C required an overpotential of 47 mV at a current density of -10 mA cm⁻² and a Tafel slope of 33 mV dec⁻¹, which are comparable to values reported in literature [27, 28].

Interestingly, the results show that the addition of Mo leads to a remarkable improvement in catalytic activity, particularly for MS2-Mo. At a current density of -10 mA cm⁻², the overpotential increased in the following order: MS2-Mo (187 mV) < MS2 (309 mV) < MS-Mo (335 mV) < MS (360 mV). A comparison of the HER activities for the HES materials is presented in table S2. At higher current densities (50 and 100 mA cm⁻²), this order remained largely the same; only the overpotential of MS2 slightly surpassed that of MS-Mo from approximately 80 mA cm⁻² on. Nevertheless, the overpotential for any given current density is higher for all HESs materials compared to Pt/C. In summary, the combination of certain specific HES structures (*Pa-3* structure instead of *Pnma*) and Mo has a significant influence on the catalytic activity.

In particular, the positive influence of Mo was also evident in the Tafel slope. For both monosulfides and disulfides, the incorporation of Mo resulted in a significant decrease in the Tafel slopes (figure 2(b)). MS2-Mo and MS-Mo (96 and 100 mV dec⁻¹, respectively) have significantly lower slopes compared to the Mo-free HES counterparts, MS and MS2 (109 and 164 mV dec⁻¹, respectively). In general, a lower Tafel slope corresponds to faster kinetics. In other words, the lower the Tafel slope, the easier the electron transfer and electron migration during the catalysis process. In order to investigate the observed HER activities in more detail, EIS measurements were performed (figure 2(c)). In the Nyquist plot, the semicircles at lower frequencies correspond to the charge transfer resistance, with MS2-Mo having the smallest semicircle, indicating the lowest impedance and fastest charge transfer among all HESs, thus correlating with its superior HER performance.

Considering that the HER performance strongly depends on the surface area of the catalyst, the ECSA was determined using C_{d1} estimated by CV measurements with different scan rates in the non-faradaic region (figures 2(d) and S3). The C_{d1} values of MS, MS-Mo, MS2 and MS2-Mo are 4.4, 5.5, 7.6 and 24.5 mF cm⁻², respectively, resulting in corresponding ECSA values of 110, 137.5, 190 and 612.5 cm², respectively.

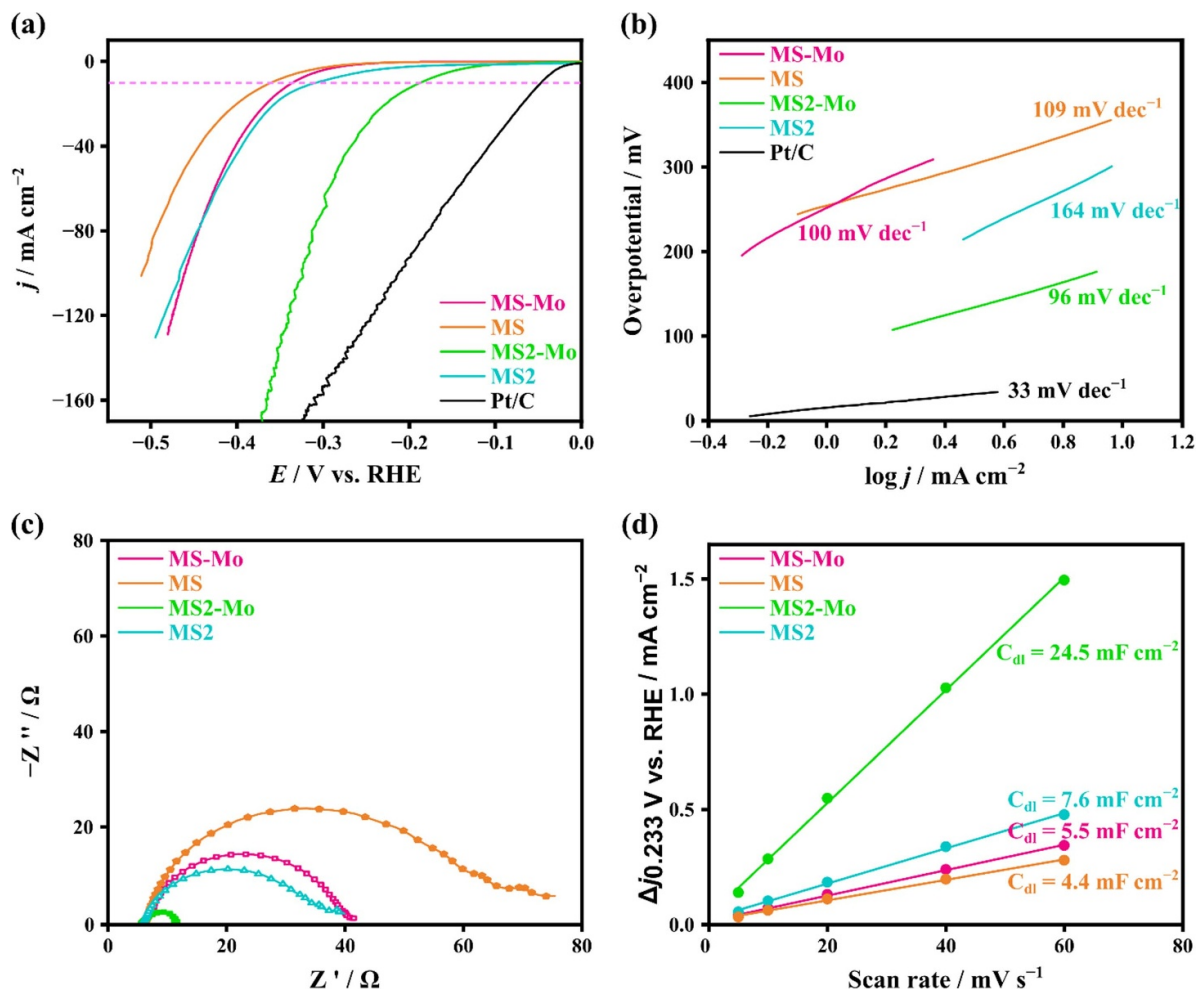


Figure 2. (a) Polarization curves of all HESs and commercial Pt/C as reference in a three-electrode cell with N_2 -saturated 1M KOH electrolyte. The pink dashed lines mark the current density of -10 mA cm^{-2} . (b) Tafel slopes derived from corresponding polarization curves. (c) Electrochemical impedance spectroscopy (EIS) results of all HESs. (d) Current density differences (Δj) of all HESs from CV curves (figure S3) plotted against the scan rate. Double-layer capacitance C_{dl} is equivalent to linear slope.

The LSV curves were normalized to the ECSA, showing that MS2-Mo has also the best intrinsic catalytic activity (figure S4). The significantly larger ECSA of MS2-Mo compared to the other HESs could probably be one of the main reasons for its enhanced catalytic performance. This is because the ECSA is the area of the electrode material that is accessible to the electrolyte and is used for charge transfer. This would also explain why MS2-Mo also outperforms MS-Mo (same metal composition). The influence of ECSA could also be illustrated using other material classes [29, 30]. In the study by Einert *et al* it was shown that, taking the ECSA into account, the improved catalytic activity of the mesoporous high-entropy spinel oxide $(Cr_{0.2}Mn_{0.2}Fe_{0.2}Co_{0.2}Ni_{0.2})_3O_4$ can be attributed primarily to the significantly increased number of catalytically active sites.

The question arises why MS2-Mo shows such improved performance compared to all other tested materials. Important material parameters that could potentially improve catalytic activity are surface, morphology and oxidation states.

Therefore, the Mo containing materials with a special focus on MS2-Mo, were further investigated.

As catalytic performances predominantly rely on surface reactions, the structural and electronic/chemical properties of the catalyst surface play a defining role. In this context, XPS was used to determine the chemical and oxidation states of elements on the surface of MS-Mo and MS2-Mo. XPS analysis provides crucial information about the valence states of various elements on the sample surface. These valence states play an important role in determining catalytic properties. In systems with multiple elements, these states can reveal synergistic effects, where the presence of one element in a specific oxidation state enhances the catalytic performance of another element.

The survey spectra (figure 3(a)) show the presence of various species on the surface of both samples, including manganese (Mn 2p), iron (Fe 2p), cobalt (Co 2p), nickel (Ni 2p), molybdenum (Mo 3d), sulfur (S 2p), and oxygen (O 1s), in addition to carbon (C 1s). The high-resolution spectra for the

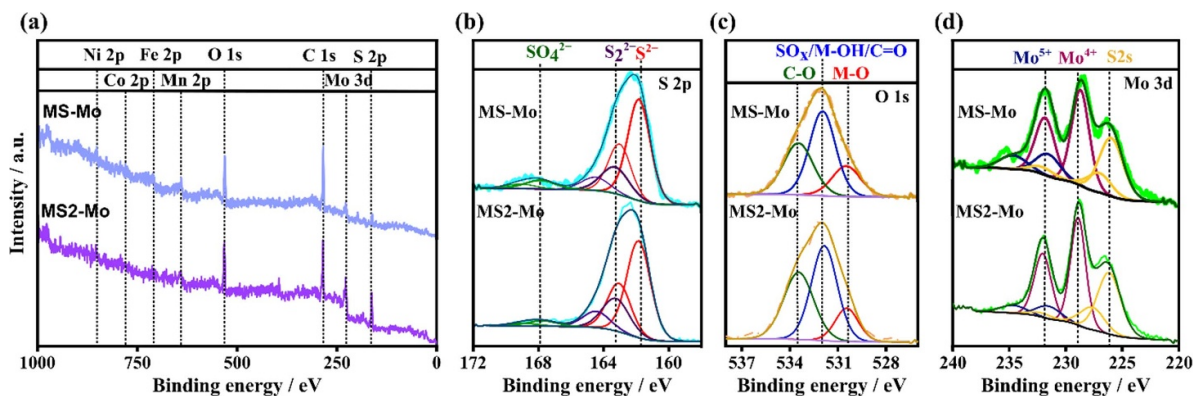


Figure 3. (a) XPS survey and high-resolution spectra in the (b) S2p, (c) O 1s and (d) Mo3d regions of MS-Mo and MS2-Mo.

S 2p, Mo 3d and O 1s regions are shown in figures 3(b)–(d), while the detail scans for Fe 2p, Co 2p, Mn 2p and Ni 2p can be found in figure S5.

The S 2p spectra (figure 3(b)) show three peak doublets for both samples. As expected, the peak doublet of sulfide species (S^{2-} , $S_{2p_{3/2}}$ at 161.6 eV) dominates the spectrum of MS-Mo. Additionally, smaller contributions are observed at higher binding energy, which can be assigned to disulfide (S_2^{2-} , $S_{2p_{3/2}}$ at 162.6 eV) and oxidized sulfur species (SO_x , $S_{2p_{3/2}}$ at 167.7 eV), respectively. Conversely, the disulfide peak doublet is the major contribution in the spectrum of MS2-Mo. These results are in good agreement with findings for other metal sulfides [31, 32]. The presence of oxidized sulfur species at the surface of MS-Mo and MS2-Mo particles is thus demonstrated. All samples display one peak at a high binding energy (≈ 533.5 eV) attributed to a C–O environment (figure 3(c)). Furthermore, the detection of a peak at 530.4 eV in the O 1s spectra for both samples indicates the presence of metal oxide (M–O) species in the surface region. These species are most probably related to an interaction of the samples with oxygen traces during preparation, storage or the process of transferring to the XPS analysis. The main peak at around 532 eV can be attributed to a mixture of oxygen from SO_x compounds, C=O, and M–OH (metal hydroxides).

The Mo 3d high-resolution spectra (figure 3(d)) show peak doublets representing two Mo species, apart from the three S 2s peaks related to S^{2-} , S_2^{2-} and SO_x . The first doublet (Mo 3 $d_{5/2}$ at 228.7 eV) could be assigned to Mo^{4+} species present as sulfide and/or oxide. Furthermore, the presence of Mo^{5+} species could be confirmed by the second doublet (Mo 3 $d_{5/2}$ at 231.5 eV) [33, 34]. The analysis of the other transition metals (Mn 2p, Fe 2p, Co 2p and Ni 2p; figures S5(a)–(d)) is complicated by multiplet splitting effects and overlap with Auger features [35]; we therefore refrained from a peak fit and will only briefly discuss the shape and position of the spectra. The spectra in the Mn 2p region contain a Ni Auger feature, which overlaps with the Mn $2p_{3/2}$ peak. As a consequence, the Mn $2p_{1/2}$ peak was used for comparison instead, which was detected for both samples at ~ 653.5 eV. Taking into account the spin-orbit splitting of the Mn 2p peak doublet ($\Delta = 11.7$ eV), this translates to a Mn $2p_{3/2}$ peak position

of 641.8 eV indicating an intermediate oxidation state, probably Mn^{3+} [20]. For Co and Ni, the position of the main $2p_{3/2}$ peaks is similar for both samples (Co $2p_{3/2}$ at ~ 779 eV, Ni $2p_{3/2}$ at ~ 853.5 eV). The observed peak positions as well as the detection of the satellite feature at ~ 787 eV in the case of Co, point to a preferred oxidation state of +2 for these two metals. Finally, the low intensity of the Fe 2p peak doublet and the presence of Co and Ni Auger features overlapping with the Fe $2p_{3/2}$ peak render an accurate analysis of the results in this region difficult. The enhanced catalytic effect of Mo-containing catalyst materials can be attributed to the introduction of Mo^{4+} as an adsorption site for reactants, which overcomes the insufficient affinity of Ni^{2+} in sulfide to water and thus facilitates the onset of HER. Thus, the Mo^{4+} sites control the adsorption of the reactant and subsequently cooperate with the nearby Ni sites to promote the dissociation of reactants, the formation of intermediates and the desorption of products during the reaction process. This behavior has been corroborated by in-situ characterization and theoretical studies of Mo^{4+} doped NiS [36]. Given that the Mo-containing HEM studied here also exhibited significantly improved catalytic performance, it is reasonable to infer that a similar mechanism is likely operating in this case as well.

Furthermore, the higher stability of MoS_x units can be combined with the higher activity of building blocks such as CoS_x to develop a robust and efficient HES system. The study by Staszak-Jirkovský *et al* suggests that Co^{2+} is about five times more stable in $CoMoS_x$ than in CoS_x , while Mo^{4+} is almost equally stable in $CoMoS_x$ and MoS_x . This indicates that the Co-based building blocks can be stabilized in the $CoMoS_x$ structure. In $CoMoS_x$ materials, the HER occurs simultaneously at the active Co^{2+} and Mo^{4+} centers. However, due to the higher instability of the Co^{2+} cations, the density of the active Co^{2+} centers is higher, so that they contribute more to the measured current density. It can therefore be assumed that the introduction of Mo into the HEM also improves the catalytic efficiency by stabilizing the structure and providing additional active sites for the reaction [37]. To gain further insights into possible functional groups in the case of HESs, the materials were analyzed using ATR-IR (figure S6). All HESs exhibited a comparable IR pattern. The absorption

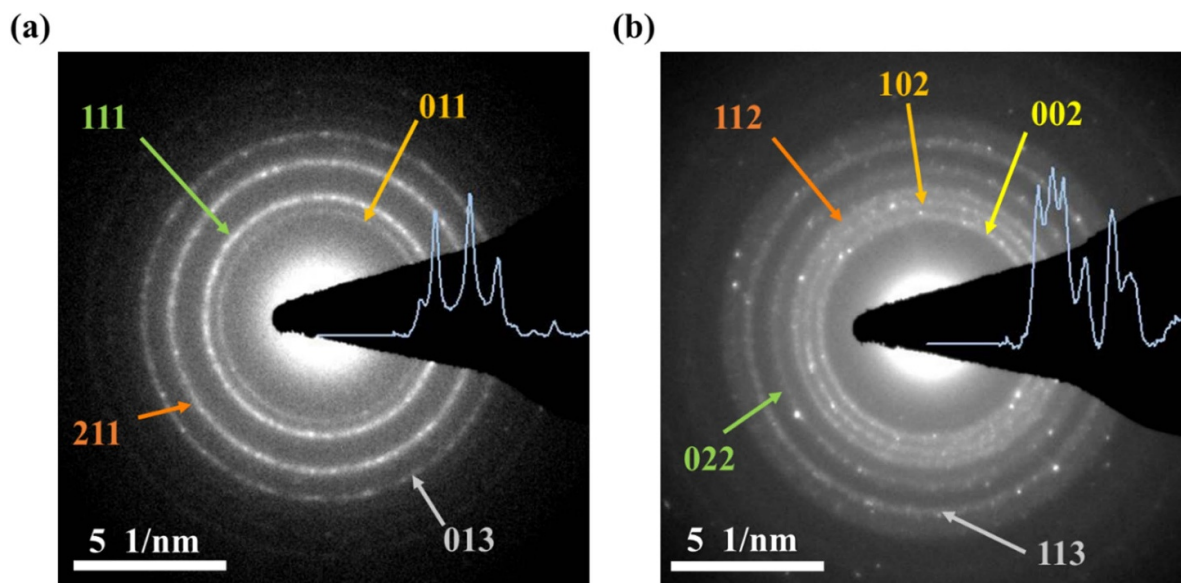


Figure 4. SAED pattern of (a) MS-Mo and (b) MS2-Mo. The diffraction rings observed for MS-Mo and MS2-Mo are consistent with the space group $Pnma$ and $Pa-3$, respectively.

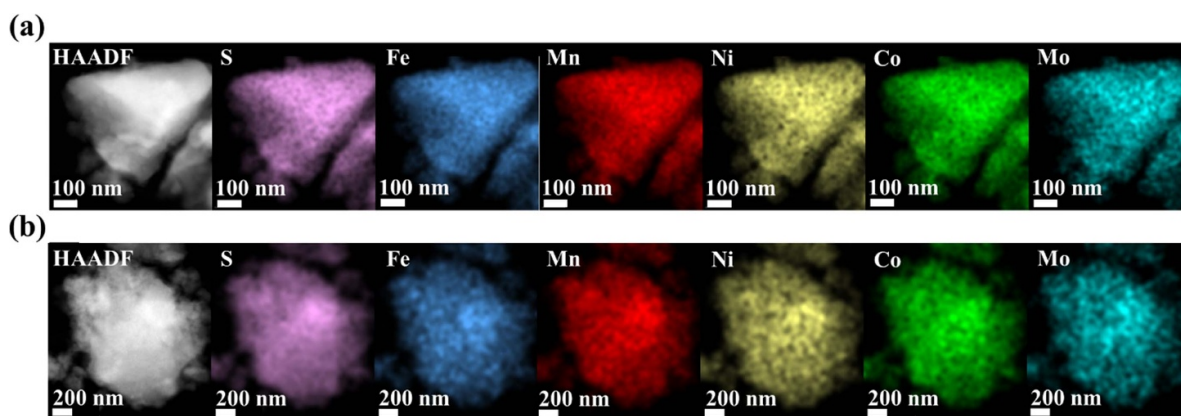


Figure 5. STEM-EDX mapping of (a) MS-Mo and (b) MS2-Mo.

bands observed in the range of $600\text{--}750\text{ cm}^{-1}$ can be attributed to metal-S stretching vibrations [38–42]. In contrast, the bands in the range of approximately $750\text{--}1600\text{ cm}^{-1}$ can be associated with sulfate and carboxyl groups, while the peak at 3400 cm^{-1} corresponds to O-H stretching [43–45]. The presence of carboxyl and O-H stretching is likely due to reactions with atmospheric air. To further investigate the surface structure, morphology and elemental distribution, TEM measurements were carried out. The high resolution TEM (HR-TEM) micrographs show irregularly shaped agglomerated particles with sizes ranging in the hundreds of nanometers (figure S7). Furthermore, the diffraction rings observed using SAED measurements (figure 4) for MS-Mo and MS2-Mo are consistent with the $Pnma$ and $Pa-3$ space groups, respectively, which aligns with the XRD data (table S3).

Figure 5 shows the STEM-EDX mapping results, which were acquired to examine the nanoscale distribution of elements in MS-Mo and MS2-Mo. The data indicate a

homogenous distribution of all elements, without observable segregation or aggregation.

HR-TEM micrographs and the corresponding fast Fourier transform (FFT) images of MS-Mo and MS2-Mo (figure 6) demonstrate a high crystallinity of the particles. In the higher magnification of the regions defined by the white squares, the red circled area in figure 6(a) corresponds to (111) lattice planes in $Pnma$ -structured MS-Mo with lattice spacing of 0.26 nm, while the blue circled area in figure 6(b) refers to (002) lattice planes in $Pa-3$ -structured MS2-Mo with spacing of 0.27 nm. Additionally, compared to the HR-TEM images of MS-Mo (figure 6(a)) or MS and MS2 (figure S8, see also [19]), sample MS2-Mo displays another feature, namely a layered structure of the material (certain layers are highlighted by yellow arrows in figure 6(b)). As can be seen, the yellow lines denote stacked MS2-Mo, revealing an interlayer distance of 0.62 nm, which is similar to the HR-TEM results of MoS₂ nanosheets reported in literature [46–49]. This result

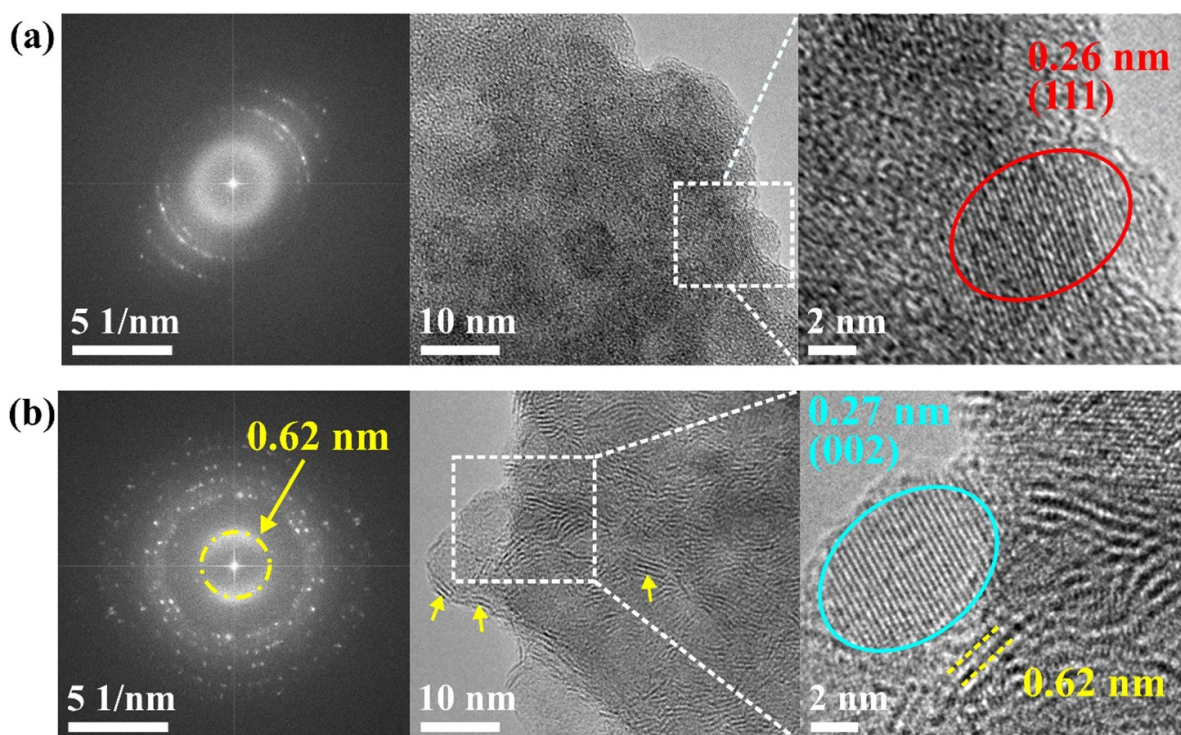


Figure 6. HR-TEM images with crystal lattices and corresponding FFT patterns of (a) MS-Mo and (b) MS₂-Mo. The layered structure of MS₂-Mo is indicated by the yellow lines and arrows.

emphasizes the unique features in HEMs that can appear due to cocktail effects. With the introduction of only approximately 20 mol. % of Mo (in relation to the other transition metals), the *Pa-3* structure was maintained, but a feature of MoS₂, the layered structure (highlighted by the yellow lines and arrows, figure 6(b)), was adapted, rendering MS₂-Mo as a unique material in our study of HESs.

The layered structure can thus be considered as one of the key factors contributing to the enhanced catalytic activity of Mo-containing HES-materials. HR-TEM images reveal that this structure is segmented into multiple sections, suggesting increased exposure of edge sites (figure 6(b)). These 'breaks' likely lead to a greater number of active sites, improving hydrogen adsorption and accelerating the HER.

The enhanced HER performance of the Mo-containing high-entropy disulfide (MS₂-Mo), compared to non-Mo HEMs, can probably be attributed to two primary factors: the formation of a layered structure and enhanced defect generation. Molybdenum plays a crucial role in facilitating the formation of the S-Mo-S layered structure, which is more prone to exfoliation and fracture. This, in turn, exposes more active edge sites that are critical for the HER process. In contrast, non-Mo disulfides, lacking this layered configuration, limit the availability of such active sites, leading to lower catalytic efficiency.

The superior performance of MS₂-Mo compared to high-entropy Mo-containing sulfide (MS-Mo) can be further explained by the presence of microfissured layers in MS₂-Mo, which are absent in MS-Mo. It can be inferred that the metal-to-sulfur ratio is the responsible factor in driving the

formation of these layered structures. In MS₂-Mo, the appropriate metal-to-sulfur ratio results in weaker van der Waals forces between the layers, facilitating interlayer separation and promoting the development of a layered structure [50]. Conversely, in MS-Mo, an improper metal-to-sulfur ratio may strengthen the chemical bonds between the layers, tightening interlayer interactions and thus preventing the formation of a layered configuration. The incorporation of molybdenum introduces advantageous structural features into HEMs, resulting from cocktail effects. This is particularly notable in cases where Mo enables the formation of a layered structure that would not typically occur in such compositions. To the best of our knowledge, this is the first time this structural adaptation has been observed in HESs. Overall, these findings underscore the critical role of molybdenum, the metal-to-sulfur ratio, and high-entropy concept in enhancing the structural and catalytic properties of HES materials. The ability to tune the metal-to-sulfur ratio offers a pathway to optimize both the structural configuration and catalytic performance, particularly in HER applications. This study highlights the importance of controlling composition to harness the full potential of high-entropy systems in electrocatalysis.

The layered structure, which emerges only due to the introduction of Mo into the HEM, leads to an increased surface area and consequently enhances catalytic performance. This phenomenon can be linked to the cocktail effects, where modifying just one element in the overall composition (as in the case of MS₂ compared to MS₂-Mo) has a significant positive impact on the material's properties. This underlines the promising role of the HEMs in catalytic applications, since using

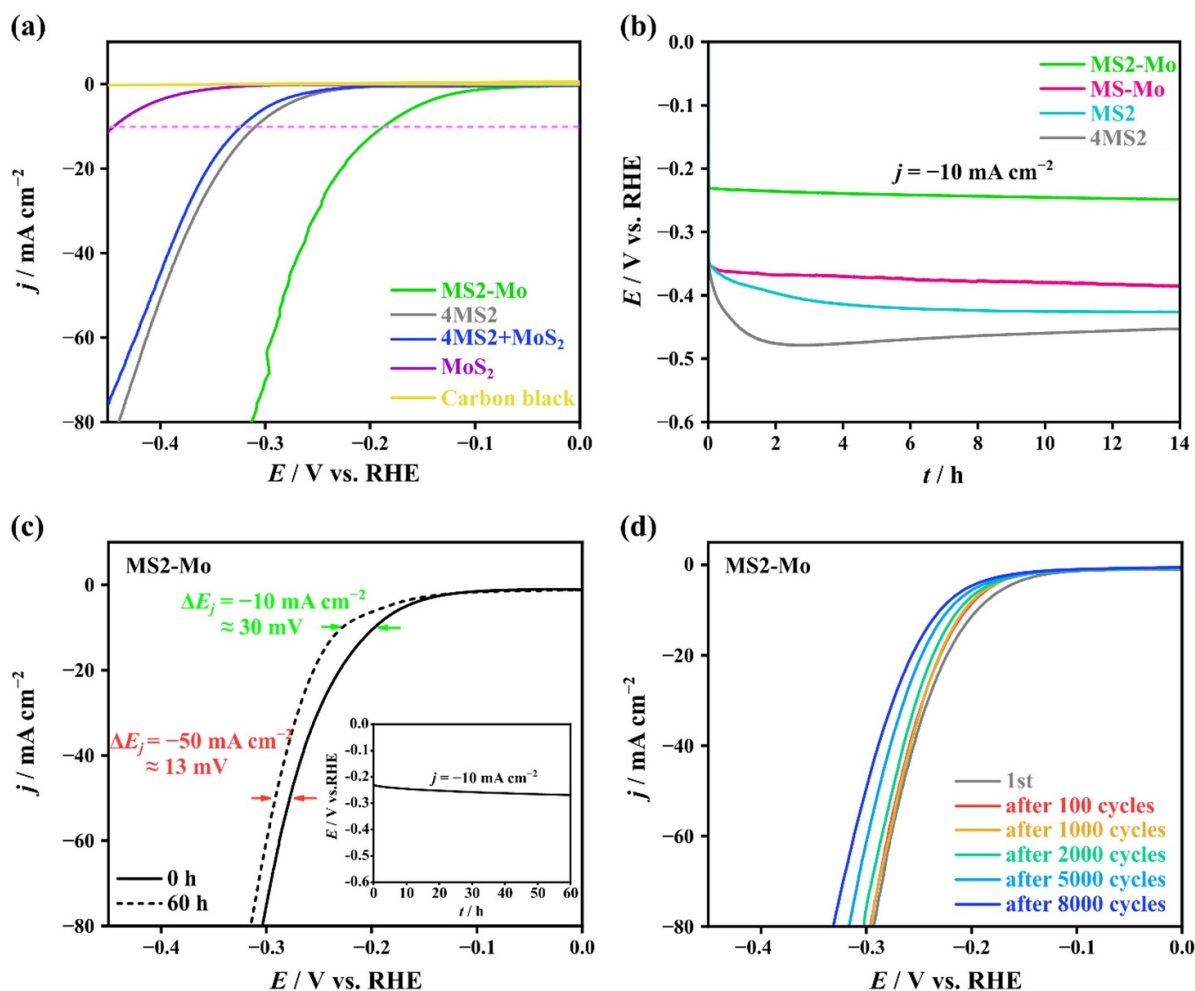


Figure 7. (a) Polarization curves of MS2-Mo, 4MS2, a mixture of 4MS2 and MoS₂, MoS₂, and carbon black in a three-electrode cell with N₂-saturated 1M KOH electrolyte. The pink dashed lines mark the current density of -10 mA cm^{-2} . (b) Chronopotentiometry curves of MS2-Mo, MS2, MS-Mo and 4MS2 for 14 h at constant current density of -10 mA cm^{-2} . (c) Polarization curves of MS2-Mo before and after 60 h chronopotentiometry at constant current density of -10 mA cm^{-2} . Inset is the corresponding chronopotentiometry curve of MS2-Mo for 60 h. (d) Polarization curves of MS2-Mo before and after 100, 1000, 2000, 5000, and 8000 CV cycles.

this approach, formerly unknown materials with elements in unconventional structural and electronic environments can be prepared, tailored, and utilized.

At this point, we would like to emphasize once again that the HESs (MS, MS2, MS-Mo and MS2-Mo) do not form layered structures per se due to their orthorhombic and cubic crystal structure. However, evidence of a layered structure can be found in the case of MS2-Mo and is probably primarily due to the incorporation of Mo. Small areas with layered structures have formed, similar to the layered MoS₂ material.

To verify this assumption, MS2-Mo (best performing HER material) is compared with the MES 4MS2, commercial MoS₂, and a mixture of 4MS2 with MoS₂. Figure 7 shows the comparison of HER catalyst performance of these materials. More precisely, the LSV curves of high-entropy MS2-Mo, medium-entropy 4MS2, commercial MoS₂, a grounded mixture of MoS₂ and 4MS2 to simulate the same elemental composition as MS2-Mo but without introducing the elements into a single-phase compound, and carbon black are shown in figure 7(a).

Although the MES 4MS2 shares the same crystal structure (space group = $Pa\bar{3}$) and similar composition (Fe, Co, Ni, Mn, S except for Mo) as MS2-Mo, it exhibits significantly higher overpotential of 309 mV at a current density of -10 mA cm^{-2} compared to the HEM MS2-Mo (187 mV at -10 mA cm^{-2}). Similarly, commercial MoS₂ features a much higher overpotential (443 mV at -10 mA cm^{-2}). Even when 4MS2 is thoroughly ground with commercial MoS₂, resulting in a mixture (4MS2 + MoS₂) with the same elemental composition and ratio as MS2-Mo, it shows an overpotential of 322 mV at -10 mA cm^{-2} . While this value is close to that of 4MS2, it remains much higher than that of MS2-Mo.

Since catalytic stability under harsh conditions is a further critical factor for HER application, the stability of the HESs (MS2-Mo, MS-Mo, and MS2) and the MES (4MS2) was investigated using chronopotentiometry measurements, the results are shown in figure 7(b). Compared to the HESs, the potential of the MES 4MS2 changes significantly in the first two hours ($\Delta E = 130 \text{ mV}$). In addition, MS2-Mo ($\Delta E = 17 \text{ mV}$ in 14 h) shows a much more stable behavior

than MS2 ($\Delta E = 80$ mV in 14 h) with the same *Pa-3* structure due to the incorporation of Mo. Interestingly, the *Pnma*-structured MS-Mo ($\Delta E = 38$ mV in 14 h), which also contains Mo, shows better stability than MS2, suggesting that the introduction of Mo significantly improves the stability of HES catalysts in an alkaline environment. In addition, the potential of MS2-Mo increases less than that of MS-Mo with the same metal composition, implying that here the crystal structure of *Pa-3* has higher catalytic stability than *Pnma*.

As MS2-Mo exhibited superior HER performance in terms of overpotential, impedance, and stability, the stability tests were extended. In figure 7(c), the results of a 60 h chronopotentiometry measurement at a constant current density of -10 mA cm $^{-2}$, along with the LSV curves before and after the 60 h long-term stability test, are shown.

MS2-Mo demonstrates outstanding long-term stability with a minimal increase in overpotential (ΔE at -10 mA cm $^{-2} = 30$ mV and ΔE at -50 mA cm $^{-2} = 13$ mV) after 60 h. At this point, we would like to emphasize that the stability tests were performed for 14 h and 60 h at a current density of -10 mA cm $^{-2}$, conditions relevant for solar water splitting using semiconductor photoelectrodes. To evaluate the potential of HESs from a more industrial applications perspective, the long-term stability of the best-performing material, MS2-Mo, was further assessed via chronopotentiometry at a current density of -100 mA cm $^{-2}$. A comparatively rapid drop in potential of around 70 mV was observed within the first 2 h, followed by a continuous drop of around 20 mV between 2 and 6 h. Subsequently, the potential showed a less pronounced decrease of around 10 mV between 6 and 14 h. Overall, the change in potential observed over the 14-hour period was $\Delta E = 100$ mV (figure S9). Furthermore, figure 7(d) shows the corresponding polarization curves of MS2-Mo after 1, 100, 1000, 2000, 5000, and 8000 CV cycles (CV cycles were performed between 0.1 V and -0.42 V vs. RHE at a scan rate of 100 mV s $^{-1}$). Compared to the initial data, the overpotentials change by 11, 12, 18, 27, 35 mV at -10 mA cm $^{-2}$ and 2, 3, 9, 22, 34 mV at -50 mA cm $^{-2}$ after 100, 1000, 2000, 5000, and 8000 CV cycles, respectively. Hence, the overpotential of MS2-Mo exhibits virtually no loss before 1000 CV cycles at high current density and shows a gradual increase before 8000 cycles, highlighting the exceptional stability of the materials in an alkaline environment. In summary, it can be stated that MS2-Mo demonstrates compared to the other HESs studied herein exceptionally high catalytic activity in terms of overpotential, impedance, kinetic, and long-term stability, underscoring the significance and benefit of the cocktail effects, which are only observed when all elements are mixed in a single-phase structure. Or in other words, with the high entropy approach we can therefore tailor future catalysts to a layer morphology and thus improve catalyst materials to which the approach can be applied.

4. Conclusion

In conclusion, we have successfully designed and synthesized two novel HESs incorporating Mo alongside four other

transition metals, utilizing a one-step facile mechanochemical synthesis under inert atmosphere. The detailed characterization of MS2-Mo with a *Pa-3* structure and MS-Mo with a *Pnma* structure was performed using XRD, ICP-OES, TEM, EDX, ATR-IR, and XPS. Remarkably, the HR-TEM analysis revealed a layered structure in MS2-Mo, a distinctive feature attributed to the incorporation of Mo. These findings exemplify the significant influence of cocktail effects in high entropy materials. The unique layered structure of MS2-Mo contributes to its significantly enhanced HER catalytic performance compared to other HESs or metal sulfide mixtures and MES. This observation underscores the advantageous transfer of a layered structure to materials that typically lack this characteristic, highlighting the versatility of the high-entropy concept. This study contributes valuable insights into the design and application of high entropy materials, paving the way for advancements in various catalytic systems. The demonstrated catalytic superiority, stability, and versatility of HESs, particularly MS2-Mo, make them promising candidates for future developments in heterogeneous catalysis.

5. Future perspectives

Building on the remarkable findings of this study, the future of HESs in electrocatalysis appears exceptionally promising. The demonstrated high performance of (Fe $_{0.2}$ Mn $_{0.2}$ Ni $_{0.2}$ Co $_{0.2}$ Mo $_{0.2}$)S $_2$ for the HER provides a solid foundation for further exploration of HESs in various catalytic applications. Future research should focus on expanding the compositional space of HESs to fine-tune their electronic and structural properties for enhanced catalytic activity and stability. In this context, high-throughput screening methods could be a promising approach to explore the broad compositional space for potential HES candidates.

The inclusion of computational modeling and machine learning could also accelerate the discovery of new HES compositions with optimal properties for HER and other catalytic processes. Additionally, investigating the integration of HESs with other functional materials, such as conductive polymers or carbon-based supports, could lead to the development of hybrid catalysts with synergistic effects, further improving their efficiency and durability.

In summary, future research in the field of HESs should aim at a comprehensive understanding and optimization of their catalytic properties, scalable synthesis methods, and integration with other advanced materials. This approach will pave the way for the next generation of efficient and durable catalysts for sustainable energy solutions.

Data availability statement

The data supporting this article have been included as part of the Supplementary Information. The original TEM data can be accessed via the following link: [10.35097/wqvj9mu0xfa94vvg](https://doi.org/10.35097/wqvj9mu0xfa94vvg).

Acknowledgment

The authors thank Florian Strauss (Karlsruhe Institute of Technology) for introduction to and assistance with the ATR-IR technique. L L acknowledges financial support from the China Scholarship Council (CSC). Z D acknowledges the Karlsruhe Nano Micro Facility at Karlsruhe Institute of Technology for providing TEM access. G K and M F gratefully acknowledge the financial support by the Deutsche Forschungsgemeinschaft (DFG, German Research Foundation) under Germany's Excellence Strategy—EXC 2154—Project No. 390874152. J A-H, B B and S S acknowledge financial support from the KIT via the project Auto.MAP and the Helmholtz Program 'Materials Systems Engineering' under Program No. 43.31.01.







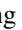

Author contributions

L L conceptualization, optimized and prepared the samples, performed x-ray diffraction, SEM and catalysis experiments, wrote the original draft. Z D performed and analyzed the SEM experiments. G K and T D performed and analyzed the XPS experiments. D-H C performed data analysis and revised the manuscript. M F, H H and J A-H revised the manuscript. B B and S S: conceptualization, writing—original draft, writing—review & editing, supervision.

Conflict of interest

The authors declare no conflicts of interests.

ORCID iDs

Ling Lin  <https://orcid.org/0000-0001-6013-2548>
 Ziming Ding  <https://orcid.org/0000-0003-4760-7806>
 Guruprakash Karkera  <https://orcid.org/0000-0002-3826-7005>
 Thomas Diemant  <https://orcid.org/0000-0001-9701-9995>
 Dong-Hui Chen  <https://orcid.org/0000-0003-2561-2444>
 Maximilian Fichtner  <https://orcid.org/0000-0002-7127-1823>
 Horst Hahn  <https://orcid.org/0000-0001-9901-3861>
 Ben Breitung  <https://orcid.org/0000-0002-1304-3398>
 Simon Schweidler  <https://orcid.org/0000-0003-4675-1072>

References

- [1] Li L, Wang P, Shao Q and Huang X 2020 Metallic nanostructures with low dimensionality for electrochemical water splitting *Chem. Soc. Rev.* **49** 3072–106
- [2] Joo J, Kim T, Lee J, Choi S I and Lee K 2019 Morphology-controlled metal sulfides and phosphides for electrochemical water splitting *Adv. Mater.* **31** 1806682
- [3] Wu Z P, Lu X F, Zang S Q and Lou X W 2020 Non-noble-metal-based electrocatalysts toward the oxygen evolution reaction *Adv. Funct. Mater.* **30** 1910274
- [4] Zhu J, Hu L, Zhao P, Lee L Y S and Wong K-Y 2020 Recent advances in electrocatalytic hydrogen evolution using nanoparticles *Chem. Rev.* **120** 851–918
- [5] Ding Q, Song B, Xu P and Jin S 2016 Efficient electrocatalytic and photoelectrochemical hydrogen generation using MoS₂ and related compounds *Chem* **1** 699–726
- [6] Li Y, Yin Z, Cui M, Liu X, Xiong J, Chen S and Ma T 2021 Interface engineering of transitional metal sulfide–MoS₂ heterostructure composites as effective electrocatalysts for water-splitting *J. Mater. Chem. A* **9** 2070–92
- [7] Su Sun Y, Alimohammadi F, Zhang D and Guo G 2017 Enabling colloidal synthesis of edge-oriented MoS₂ with expanded interlayer spacing for enhanced HER catalysis *Nano Lett.* **17** 1963–9
- [8] Li G *et al* 2016 All the catalytic active sites of MoS₂ for hydrogen evolution *J. Am. Chem. Soc.* **138** 16632–8
- [9] Cui M, Yang C, Li B, Dong Q, Wu M, Hwang S, Xie H, Wang X, Wang G and Hu L 2021 High-entropy metal sulfide nanoparticles promise high-performance oxygen evolution reaction *Adv. Energy Mater.* **11** 1–8
- [10] Nguyen T X, Su Y, Lin C and Ting J 2021 Self-reconstruction of sulfate-containing high entropy sulfide for exceptionally high-performance oxygen evolution reaction electrocatalyst *Adv. Funct. Mater.* **31** 2106229
- [11] Lin L *et al* 2023 High-entropy sulfides as highly effective catalysts for the oxygen evolution reaction *Small Struct.* **4** 2300012
- [12] Shi J, Jiang H, Hong X and Tang J 2024 Non-noble metal high entropy sulfides for efficient oxygen evolution reaction catalysis *Appl. Surf. Sci.* **642** 158598
- [13] Wang P, Wang G, Chen K, Pan W, Yi L, Wang J, Chen Q, Chen J and Wen Z 2023 High-power hybrid alkali-acid fuel cell for synchronous glycerol valorization implemented by high-entropy sulfide electrocatalyst *Nano Energy* **118** 108992
- [14] Lei Y, Zhang L, Xu W, Xiong C, Chen W, Xiang X, Zhang B and Shang H 2022 Carbon-supported high-entropy Co-Zn-Cd-Cu-Mn sulfide nanoarrays promise high-performance overall water splitting *Nano Res.* **15** 6054–61
- [15] Xiao W *et al* 2023 Synthesis of high entropy and entropy-stabilized metal sulfides and their evaluation as hydrogen evolution electrocatalysts *Chem. Mater.* **35** 7904–14
- [16] Hasanvandian F, Zehtab Salmasi M, Moradi M, Farshineh Saei S, Kakavandi B and Rahman Setayesh S 2022 Enhanced spatially coupling heterojunction assembled from CuCo₂S₄ yolk-shell hollow sphere encapsulated by Bi-modified TiO₂ for highly efficient CO₂ photoreduction *Chem. Eng. J.* **444** 136493
- [17] Hasanvandian F, Fayazi D, Kakavandi B, Giannakis S, Sharghi M, Han N and Bahadoran A 2024 Revitalizing CO₂ photoreduction: fine-tuning electronic synergy in ultrathin g-C₃N₄ with amorphous (CoFeNiMnCu)₂ high-entropy sulfide nanoparticles for enhanced sustainability *Chem. Eng. J.* **496** 153771
- [18] Li Y *et al* 2021 Recent advances in waste water treatment through transition metal sulfides-based advanced oxidation processes *Water Res.* **192** 116850
- [19] Lin L *et al* 2022 High-entropy sulfides as electrode materials for li-ion batteries *Adv. Energy Mater.* **12** 2103090
- [20] Moulder J F and Chastain J 1992 *Handbook of x-ray Photoelectron Spectroscopy: A Reference Book of Standard Spectra for Identification and Interpretation of XPS Data* (Perkin-Elmer)
- [21] Enyashin A N, Yadgarov L, Houben L, Popov I, Weidenbach M, Tenne R, Bar-Sadan M and Seifert G 2011 New route for stabilization of 1T-WS₂ and MoS₂ phases *J. Phys. Chem. C* **115** 24586–91
- [22] Wang S, Zhang D, Li B, Zhang C, Du Z, Yin H, Bi X and Yang S 2018 Ultrastable in-plane 1T–2H MoS₂ heterostructures for enhanced hydrogen evolution reaction *Adv. Energy Mater.* **8** 1801345

- [23] Lei Z, Zhan J, Tang L, Zhang Y and Wang Y 2018 Recent development of metallic (1T) phase of molybdenum disulfide for energy conversion and storage *Adv. Energy Mater.* **8** 1703482
- [24] Huang Y et al 2019 Atomically engineering activation sites onto metallic 1T-MoS₂ catalysts for enhanced electrochemical hydrogen evolution *Nat. Commun.* **10** 982
- [25] Attanayake N H, Thenuwara A C, Patra A, Aulin Y V, Tran T M, Chakraborty H, Borguet E, Klein M L, Perdew J P and Strongin D R 2018 Effect of intercalated metals on the electrocatalytic activity of 1T-MoS₂ for the hydrogen evolution reaction *ACS Energy Lett.* **3** 7–13
- [26] Tang Q and Jiang D 2016 Mechanism of hydrogen evolution reaction on 1T-MoS₂ from first principles *ACS Catal.* **6** 4953–61
- [27] Lang X, Qadeer M A, Shen G, Zhang R, Yang S, An J, Pan L and Zou -J-J 2019 A Co–Mo₂N composite on a nitrogen-doped carbon matrix with hydrogen evolution activity comparable to that of Pt/C in alkaline media *J. Mater. Chem. A* **7** 20579–83
- [28] Liu W, Ji J, Yan X, Liu W, Huang Y-C, Wang K, Jin P, Yao X and Jiang J 2020 A cascade surface immobilization strategy to access high-density and closely distanced atomic Pt sites for enhancing alkaline hydrogen evolution reaction *J. Mater. Chem. A* **8** 5255–62
- [29] Einert M, Mellin M, Bahadorani N, Dietz C, Lauterbach S and Hofmann J P 2022 Mesoporous high-entropy oxide thin films: electrocatalytic water oxidation on high-surface-area spinel (Cr_{0.2}Mn_{0.2}Fe_{0.2}Co_{0.2}Ni_{0.2})₃O₄ electrodes *ACS Appl. Energy Mater.* **5** 717–30
- [30] Schweidler S et al 2022 Synthesis of perovskite-type high-entropy oxides as potential candidates for oxygen evolution *Front. Energy Res.* **10** 983979
- [31] Ali T, Qiao W, Zhang D, Liu W, Sajjad S, Yan C and Su R 2021 Surface sulfur vacancy engineering of metal sulfides promoted desorption of hydrogen atoms for enhanced electrocatalytic hydrogen evolution *J. Phys. Chem. C* **125** 12707–12
- [32] Yu L, Cui W-G, Zhang Q, Li Z-F, Shen Y and Hu T-L 2021 Atomic layer deposition of nano-scale molybdenum sulfide within a metal–organic framework for highly efficient hydrodesulfurization *Mater. Adv.* **2** 1294–301
- [33] Fominski V, Demin M, Nevolin V, Fominski D, Romanov R, Gritskovich M and Smirnov N 2020 Reactive pulsed laser deposition of clustered-type MoS_x (x ~ 2, 3, and 4) films and their solid lubricant properties at low temperature *Nanomaterials* **10** 653
- [34] Lee Y-J, Barrera D, Luo K and Hsu J W P 2012 *In Situ* chemical oxidation of ultrasmall MoO_x nanoparticles in suspensions *J. Nanotechnol.* **2012** 195761
- [35] Biesinger M C, Payne B P, Grosvenor A P, Lau L W M, Gerson A R and Smart R S C 2011 Resolving surface chemical states in XPS analysis of first row transition metals, oxides and hydroxides: cr, Mn, Fe, Co and Ni *Appl. Surf. Sci.* **257** 2717–30
- [36] Zhou Y, Wang Y, Kong D, Zhao Q, Zhao L, Zhang J, Chen X, Li Y, Xu Y and Meng C 2023 Revealing the reactant mediation role of low-valence mo for accelerated urea-assisted water splitting *Adv. Funct. Mater.* **33** 2210656
- [37] Staszak-Jirkovský J et al 2016 Design of active and stable Co–Mo–S_x chalcogels as pH-universal catalysts for the hydrogen evolution reaction *Nat. Mater.* **15** 197–203
- [38] da Silveira Firmiano E G, Rabelo A C, Dalmaschio C J, Pinheiro A N, Pereira E C, Schreiner W H and Leite E R 2014 Supercapacitor electrodes obtained by directly bonding 2D MoS₂ on reduced graphene oxide *Adv. Energy Mater.* **4** 1301380
- [39] Yang J X, Wang S M, Zhao X L, Tian Y P, Zhang V S Y, Jin B K, Hao X P, Xu X Y, Tao X T and Jiang M H 2008 Synthesis of CdS nanoparticles in solution and in a polyphosphazene matrix *J. Cryst. Growth* **310** 4358–61
- [40] Elango M, Gopalakrishnan K, Vairam S and Thamilselvan M 2012 Structural, optical and magnetic studies on non-aqueous synthesized CdS:Mn nanomaterials *J. Alloys Compds.* **538** 48–55
- [41] Mahieddine A, Adnane-Amara L, Tebaa T and Saba C 2023 Core-shell structured hierarchical Ni nanowires and NiS/Co₃S₄ microflowers arrays as a high-performance supercapacitor electrode *J. Energy Storage* **57** 106173
- [42] Min X, Li Y, Ke Y, Shi M, Chai L and Xue K 2017 Fe-FeS₂ adsorbent prepared with iron powder and pyrite by facile ball milling and its application for arsenic removal *Water Sci. Technol.* **76** 192–200
- [43] Zhou K, Jiang S, Bao C, Song L, Wang B, Tang G, Hu Y and Gui Z 2012 Preparation of poly(vinyl alcohol) nanocomposites with molybdenum disulfide (MoS₂): structural characteristics and markedly enhanced properties *RSC Adv.* **2** 11695–703
- [44] Teo E Y L, Ali G A M, Algarni H, Cheewasedtham W, Rujiralai T and Chong K F 2019 One-step production of pyrene-1-boronic acid functionalized graphene for dopamine detection *Mater. Chem. Phys.* **231** 286–91
- [45] Girish M, Dhandayuthapani T, Sivakumar R and Sanjeeviraja C 2015 MnS thin films prepared by a simple and novel nebulizer technique: report on the structural, optical, and dispersion energy parameters *J. Mater. Sci., Mater. Electron.* **26** 3670–84
- [46] Veeramalai C P, Li F, Liu Y, Xu Z, Guo T and Kim T W 2016 Enhanced field emission properties of molybdenum disulfide few layer nanosheets synthesized by hydrothermal method *Appl. Surf. Sci.* **389** 1017–22
- [47] Li M, Wang D, Li J, Pan Z, Ma H, Jiang Y and Tian Z 2016 Facile hydrothermal synthesis of MoS₂ nano-sheets with controllable structures and enhanced catalytic performance for anthracene hydrogenation *RSC Adv.* **6** 71534–42
- [48] Gao Y-P, Huang K-J, Wu X, Hou Z-Q and Liu Y-Y 2018 MoS₂ nanosheets assembling three-dimensional nanospheres for enhanced-performance supercapacitor *J. Alloys Compds.* **741** 174–81
- [49] Su D, Dou S and Wang G 2015 Ultrathin MoS₂ Nanosheets as Anode Materials for Sodium-Ion Batteries with Superior Performance *Adv. Energy Mater.* **5** 1401205
- [50] MacMahon D, Brothers A, Florent K and Kurinec S 2015 Layered structure of MoS₂ investigated using electron energy loss spectroscopy *Mater. Lett.* **161** 96–99